Heliyon 10 (2024) e30660

Contents lists available at ScienceDirect

Heliyon

journal homepage: www.cell.com/heliyon

Research article

Method for rock fracture prediction and early warning: Insight from fusion of multi-physics field information

Qiangqiang Gao [a], Liqiang Ma [a,b,c,d,*], Wei Liu [a], Naseer Muhammad Khan [e,f], Saad S. Alarifi [g], Mohammed Sazid [h], Waleed Bin Inqiad [i]

[a] School of Mines, China University of Mining and Technology, Xuzhou, Jiangsu, 221116, China
[b] Key Laboratory of Xinjiang Coal Resources Green Mining (Xinjiang Institute of Engineering), Ministry of Education, Urumqi, 830023, China
[c] Xinjiang Key Laboratory of Coal-bearing Resources Exploration and Exploitation, Xinjiang Institute of Engineering, Urumqi 830023, China
[d] Xinjiang Engineering Research Center of Green Intelligent Coal Mining, Xinjiang Institute of Engineering, Urumqi 830023, China
[e] Sustainable Advanced Geomechanical Engineering, Military College of Engineering, National University of Sciences and Technology, Risalpur, 23200, Pakistan
[f] MEU Research Unit, Middle East University, Amman, 11831, Jordan
[g] Department of Geology and Geophysics, College of Science, King Saud University, P.O. Box 2455, Riyadh, 11451, Saudi Arabia
[h] Mining Engineering Department King Abdulaziz University Jeddah, Saudi Arabia
[i] Department of Civil Engineering, Military College of Engineering, National University of Sciences and Technology, Risalpur, 23200, Pakistan

ARTICLE INFO

Keywords:
Multi-information fusion
Infrared radiation
Acoustic emission
Coal rock fracture
Principal component analysis (PCA)

ABSTRACT

Understanding the precursors leading to rock fracture is crucial for ensuring safety in mining and geotechnical engineering projects. To effectively discern these precursors, a collaborative monitoring approach that integrates multiple sources of information is imperative. This paper considered a rock multi-parameter monitoring loading system, incorporating infrared radiation and acoustic emission monitoring technologies to simultaneously track the rock fracture process. The study delves into the spatiotemporal evolution patterns of infrared radiation and acoustic emission in rock under loading. Utilizing stress, cumulative acoustic emission count, and average infrared radiation temperature (AIRT), the paper establishes a comprehensive evaluation model termed "acoustic-thermal-stress" fusion information, employing principal component analysis (PCA). The research reveals that the sensitivity to rock sample damage response follows the sequence of cumulative acoustic emission count, AIRT, and stress. Furthermore, a novel method for identifying rock fracture precursors is proposed, based on the first derivative of the comprehensive evaluation model. This method addresses the limitations of single physical field information, enhancing the robustness of monitoring data. It determines the average stress level of fracture precursors to be $0.77\sigma_{max}$. Subsequently, the study defines the probability function of rock damage during loading and fracture, enabling the realization of probability-based warnings for rock fracture. This approach introduces a new perspective on rock fracture prediction, significantly contributing to safety monitoring and warning systems in mine safety and geotechnical engineering. The findings of this research hold paramount engineering significance, offering valuable insights for enhancing safety measures in such projects.

* Corresponding author. School of Mines, China University of Mining and Technology, Xuzhou, Jiangsu, 221116, China.
E-mail address: ckma@cumt.edu.cn (L. Ma).

https://doi.org/10.1016/j.heliyon.2024.e30660
Received 24 February 2024; Received in revised form 14 April 2024; Accepted 1 May 2024
Available online 6 May 2024
2405-8440/© 2024 The Authors. Published by Elsevier Ltd. This is an open access article under the CC BY-NC-ND license (http://creativecommons.org/licenses/by-nc-nd/4.0/).

1. Introduction

Initiating an exploration into the deepening depths of coal mining, it's clear that mine safety production is navigating through formidable challenges. Notably, issues such as mine water inrush [1,2], rock burst [3], coal and gas outburst [4], and other dynamic disasters involving coal and rock have become more pronounced. The fundamental cause underlying these disasters lies in the heightened degree of internal damage within coal and rock formations as a consequence of mining activities. Research findings underscore that the process of coal rock damage involves the simultaneous release and alteration of various forms of energy, including acoustic emission and infrared radiation [5–8]. A crucial proposition emerges: the scientific monitoring and early warning of early-stage coal rock damage could be instrumental in effectively controlling the onset of disasters and ensuring the overall safety of production processes. Therefore, delving into the analysis and extraction of distinctive characteristics of coal rock rupture precursors from a plethora of physical field information, encompassing phenomena like acoustic emission and infrared radiation, assumes pivotal engineering significance. This pursuit stands essential for advancing the domains of mine safety and geotechnical engineering, enabling robust safety monitoring, and facilitating timely warnings to avert potential hazards.

Infrared radiation monitoring technology offers numerous advantages, including non-contact, non-destructive, real-time, cost-effectiveness, and high efficiency. As a result, researchers both domestically and internationally have embraced its application in studying rock damage, fracture monitoring, and early warning systems, yielding significant research breakthroughs [9,10]. Wu et al. [11–14] pioneered the concept of remotely sensed rock mechanics (RSRM) and presented experimental methodologies and findings regarding the correlation between infrared radiation and rock stress. Additionally, they outlined future research directions and highlighted key issues pertinent to the development of RSRM.

To comprehensively analyze the characteristics of infrared radiation precursors during rock rupture, researchers have introduced various quantitative evaluation metrics over time. These include AIRT [14,15], extreme values (maximum and minimum temperature) [16,17], variance [18], differential infrared radiation variance [19], infrared image entropy [20], b-value of infrared radiation [21], high-temperature point scaling factor [22], skewness of temperature distribution [17,23], kurtosis of temperature distribution [23], roughness [24], and others. Through these measures, scholars have identified both qualitative and quantitative traits associated with rock rupture precursors. Furthermore, investigations have been conducted to understand the influence of water on the infrared radiation temperature of load-bearing rocks. For instance, Cai et al. [25] and Shan et al. [23] conducted uniaxial compression experiments on both dry and water-saturated rocks, revealing that the presence of water enhances the release of infrared radiation energy from rocks. Moreover, Li et al. [26] explored the fluctuation patterns of infrared radiation in coal rocks under gas influence, suggesting that infrared thermograms and temperature curves can effectively predict deformation and damage in coal rocks, aiding in the precise localization of dynamic hazards within coal formations. Additionally, studies by Li et al. [26] examined the changes in infrared radiation emitted by coal rocks due to gas interactions, indicating the potential of infrared thermography in forecasting coal rock deformation and identifying areas prone to power-related disasters. Mineo et al. [27] utilized infrared thermography to indirectly assess rock porosity, while Liu et al. [28] delineated the effective infrared temperature fields associated with rock crack development. They introduced the concept of Infrared Energy Response of Damage (IERD) to characterize crack evolution within rocks and proposed an intrinsic model for rock damage. Overall, the application of infrared radiation monitoring techniques stands as a crucial tool in researching and developing precursor features essential for early prediction and warning of critical rock damage.

Acoustic emission technology is a powerful tool for detecting and locating internal cracks within coal rock formations. For instance, Ohno et al. [29] utilized acoustic emission parameters to effectively categorize the various crack patterns found in concrete structures. Similarly, Wang et al. [30] conducted research on anisotropic shale subjected to cyclic loading, uncovering its fracture modes and evolution laws, and delving into the associated failure mechanisms driven by different crack patterns. Meng et al. [31] explored the dynamics of energy accumulation, evolution, and dissipation during uniaxial cyclic loading and unloading at varying rates, analyzing the rock's stress-strain behavior and acoustic emission characteristics throughout deformation and failure processes. Furthermore, Shan et al. [32] established a quantitative relationship between dissipation energy and acoustic emission parameters in coal rock, providing clear insights into the fracture behaviors of this material. In another study, Ding et al. [33] focused on coal-rock samples, extracting distinct acoustic emission signal characteristics. They devised a stress state criterion based on these signal features and employed a BP neural network for in-depth learning of the signal properties, thereby enabling the identification, classification, and prediction of coal-rock material behavior. These collective efforts highlight the versatility and significance of acoustic emission technology in the comprehensive understanding and management of rock mechanics and materials.

Researchers have conducted extensive studies on the changes in infrared radiation and acoustic emissions during the destabilization and damage processes of coal rock [34–38]. These studies have yielded valuable insights and findings. However, relying solely on information from a single physical field may result in inadequate monitoring and low reliability in early warning systems. For instance, while infrared radiation can effectively monitor surface temperatures, it only provides limited utility in critical monitoring and warning of coal-rock disasters. Nonetheless, it offers the advantages of non-destructive, non-contact, and remote sensing capabilities [39,40]. On the other hand, acoustic emission analysis can pinpoint the internal locations of coal and rock ruptures [3,41,42], yet its effectiveness is often compromised by environmental interference, reducing its adaptability for early warning in critical disaster scenarios. Consequently, the fusion of these two sources of information for early warning analysis holds the potential to significantly enhance accuracy and reliability, offering a more robust approach to disaster prevention and mitigation [43–46].

This paper investigates the evolution characteristics of "acoustic-thermal-stress" information during the rock rupture process. It establishes a comprehensive evaluation model for the rock loading and rupture sequence, employing the principal component analysis method alongside acoustic emission cumulative ring counts, infrared radiation, and stress parameters. This analysis leads to the development of a method for identifying rock damage precursors based on the first-order derivatives of the comprehensive evaluation

model. This integrated approach harnesses the strengths of information from each physical field involved in the rock loading and rupture process, thereby enhancing the resilience of monitoring data. The proposed method introduces innovative ways and indicators for real-time observation of rock fissure development and damage, providing theoretical and experimental foundations for rock damage detection. These findings offer crucial insights for ensuring the safe and efficient execution of underground projects, including mines and tunnels.

2. Materials and methods

2.1. Sample Preparation

The sandstone used in this experiment is formed by the segmentation of the whole rock in the same direction. The sample is a cuboid standard specimen of 50 mm × 50 mm × 100 mm. The two ends are polished with sandpaper, so that the roughness error of the end face is less than 0.05 mm, and the non-parallel error of the two sides is less than 0.03 mm. A total of 5 pieces are processed and numbered A_i (i = 1, 2, …, 5).

2.2. Experimental procedure

All samples were acclimated in the laboratory for a duration of 24 h preceding the commencement of the experiment. To ensure uniformity, the acoustic emission probe was affixed to the surface of the rock specimen, aligning its temperature with that of the laboratory environment at the onset of testing. Concurrently, the infrared camera was positioned approximately 1 m ahead of the specimen, with its lens situated at the same elevation as the central point of the loaded specimen surface, as illustrated in Fig. 1. It should be noted that the infrared radiation temperature during rock loading depends upon several factors among which the ambient temperature, air humidity and rock emissivity are the most important. Thus, to minimize disturbances due to these factors, all researchers wore thermally insulated gloves throughout the experiment to prevent any thermal conduction between their body temperature and that of the rock surface. The loaded specimen was situated on the loading platform of the press, while a reference specimen of identical dimensions was placed at a horizontally aligned position, 10 cm to the left of the loaded specimen. The press was loaded at a consistent displacement rate of 0.2 mm per minute, while the infrared camera operated at an acquisition rate of 10 frames per second. Synchronization between the press and the infrared camera was meticulously maintained to facilitate data acquisition throughout the duration of the test.

In addition, the ambient temperature, air humidity and rock surface emissivity in the laboratory were recorded, which were 16 °C, 52 % and 0.82, respectively. These physical parameters are set synchronously in the thermal imager to improve the monitoring accuracy of infrared radiation temperature. In addition, all persons are prohibited from carrying out activities during the experiment until the end of the experiment. In order to prevent the thermal radiation caused by personnel walking affect the experimental results.

2.3. Experimental equipment

The experimental setup employs state-of-the-art equipment, including the MTS electro-hydraulic servo universal testing machine, renowned for its impressive maximum load capacity of 1000 kN. Complementing this machinery is the infrared thermal imaging system, specifically the VarioCAM HD head 880 model, crafted by InfraTec in Germany. This cutting-edge thermal imager stands out for its remarkable temperature measurement capabilities, spanning from −40 °C to 1200 °C, with an exceptional temperature

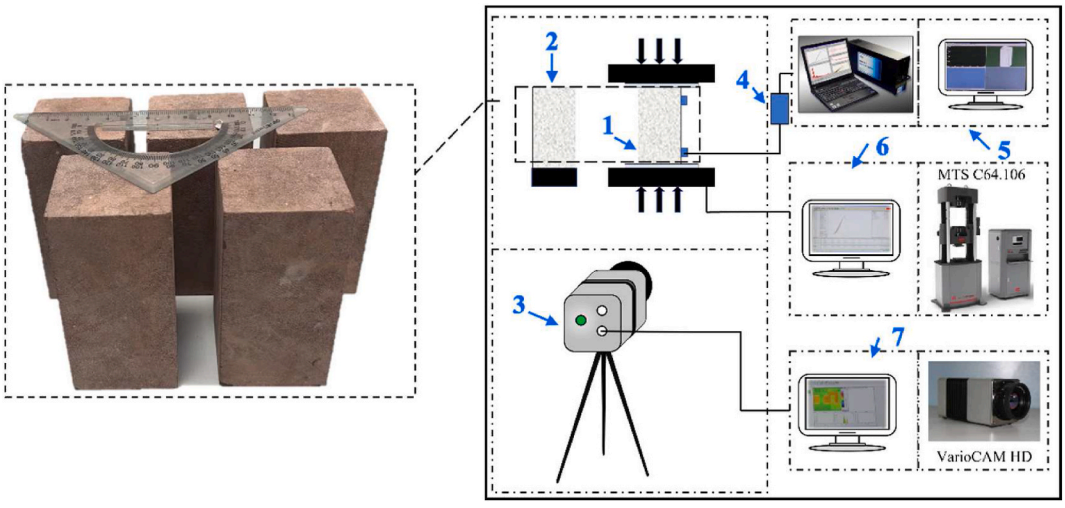

Fig. 1. Experimental schematic diagram.

sensitivity of 0.02 °C. Additionally, boasting an image resolution of 1240 × 768 pixels, it facilitates meticulous thermal analysis. Operating at a maximum image acquisition frequency of 30 frames per second, and with a measurement band extending from 7.5 to 14 μm, this thermal imager offers unparalleled precision.

Simultaneously, the experimental setup incorporates the use of an acoustic emission monitoring device, sourced from the PAC company and identified as the PCI-2 model. This advanced instrument showcases a bandwidth range spanning from 1 KHz to 3MHz. Equipped with a built-in 10-channel filter and an 18-bit A/D converter, it enables real-time monitoring and display of acoustic emission signals throughout the loading process. These sophisticated technical specifications provide researchers with the capability to capture and analyze acoustic emissions with utmost accuracy and comprehensiveness, enhancing the depth and precision of experimental data collection.

3. Experimental results and analysis

To mitigate the potential inaccuracies arising from the discrete nature of the sample, we conducted a uniaxial compression test incorporating infrared radiation and acoustic emission monitoring at ambient temperature. The resulting stress-strain curves for each individual sample can be observed in Fig. 2, providing a comprehensive depiction of the experimental outcomes.

The stress-strain evolution trends depicted in Fig. 2 exhibit striking similarity across all five specimens. Due to constraints on space within this paper, we have chosen to delve into the failure process of the A_3 sample for detailed analysis. This specimen's failure process will serve as a representative case for the broader trends observed in the experiment.

3.1. Infrared temperature data denoising

Fig. 3 presents a comprehensive flowchart delineating the denoising methodology employed in this study for infrared data. Grounded in preliminary findings that indicate the presence of both additive and multiplicative noise in rock infrared radiation data, the approach detailed in this paper integrates background denoising and wavelet threshold techniques to refine the data.

The denoising process is a meticulous sequence of operations. It commences with the subtraction of the thermal image of a reference sample from the loaded sample to perform background denoising, thereby isolating the noise inherent to the measurement environment. This is followed by the application of an adaptive median filter, which is calibrated with a window size that varies between 3 and 5 pixels to accommodate the specific features of each thermal image sequence, enhancing the denoising efficacy.

The capstone of the process is the application of one-layer wavelet decomposition to the infrared image sequence, harnessing the coif 4 wavelet basis function. This step employs wavelet soft thresholding, a technique that effectively eradicates both additive and multiplicative noise from the thermal images, yielding data of superior quality for subsequent analysis.

For an in-depth exposition of the denoising methodology, as referenced [47], Fig. 3 offers a visual synopsis that captures the essence of each procedural step, highlighting the systematic approach taken to ensure the highest fidelity in the infrared temperature field sequence data.

3.2. Temporal evolution of infrared radiation in rocks

The infrared thermograms' temperature values for each frame underwent statistical analysis to derive their average infrared radiation temperature (AIRT). This AIRT serves as a crucial indicator for gauging the surface temperature change from the initial bearing to the eventual damage of the rock specimen. The calculation method of rock AIRT is:

$$AIRT(p) = \frac{1}{m}\frac{1}{n}\sum_{x=1}^{m}\sum_{y=1}^{n}[g(x,y,p)]$$

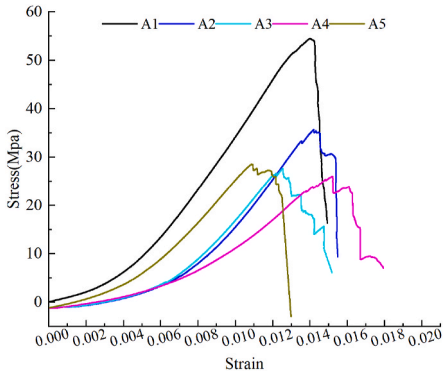

Fig. 2. Stress-strain curve diagram.

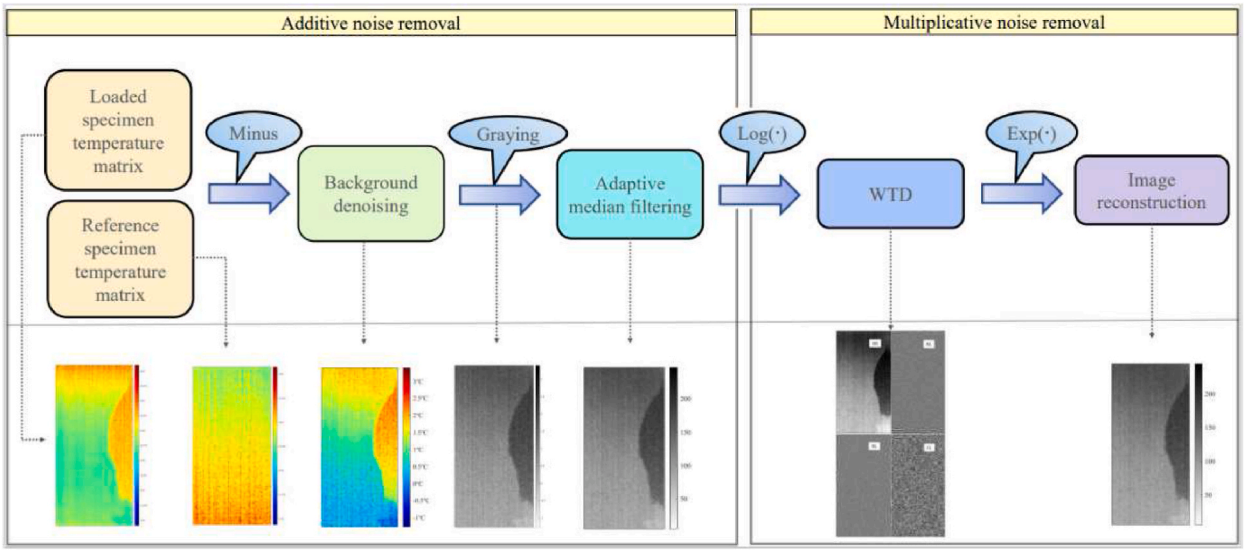

Fig. 3. Denoising process diagram.

where, g represents the bearing rock temperature matrix after de-noising, x and y represent the matrix row and column indexes, and p represents the frame index.

Illustrated in Fig. 4 is the AIRT curve plotted against stress for specimen A3, with analogous trends observed across other specimens. In the loading phase of rock specimen A3 depicted in Fig. 4, there's a distinct linear increase in AIRT, with a sudden surge upon the specimen's ultimate failure. However, the trajectory of AIRT alterations varies across different loading stages.

As shown in Fig. 4, the AIRT during the loading process of sample A3 exhibits a nearly linear upward trend. When the sample ultimately fails, there is a sudden increase in AIRT. However, the trends of AIRT variation in different loading stages are not the same. In the compaction stage (Stage I), the internal inherent fractures of the rock are gradually compacted, causing the escape of gas from internal pores, fractures, micro-cavities, etc. This gas escape process consumes some energy, thus resulting in a temporary decrease in AIRT [38]. However, as the rock is gradually stressed, internal particles and mineral crystals undergo dislocation slip and frictional heating, causing AIRT to slowly rise after a slight decline. Therefore, the variation of AIRT in this stage is mainly related to the desorption-escape effect of original gases in the rock and the frictional heating effect between particles [48]. In the stage of linear elastic deformation (Stage II), stress increases linearly with time, and the elastic deformation of the rock under uniaxial compression can be regarded as an isentropic reversible process. The physical temperature approximately linearly correlates with stress changes, hence AIRT in this stage is linearly positively correlated with stress, mainly related to the thermoelastic effect [49–52]. In the plastic deformation stage (Stage III), due to rapid development and expansion of internal cracks in the rock, which gather to form macroscopic fractures, this process is an irreversible thermodynamic process of energy dissipation. During the process of crack propagation, the initially stored elastic energy is converted into fracture energy, kinetic energy, and heat energy. Particularly in the vicinity of the crack tip region, heat is generated, leading to a local temperature rise and a rapid increase in AIRT [17,51,53]. In the post-peak deformation stage (Stage IV), before the sample structure is destroyed, cracks further develop, and AIRT continues to rise. When the sample structure becomes unstable and fails, there is a sudden increase in AIRT.

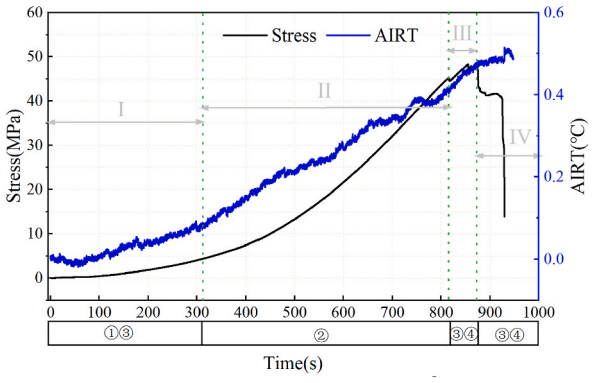

Fig. 4. Stress vs. AIRT curves of A3 specimen. ①pore gas desorption-escape effect,②thermoelastic effect, ③friction heat effect, ④crack extension heat effect.

3.3. Evolution law of acoustic emission

The cumulative ringing count index serves as a crucial tool for examining the acoustic emission characteristics during the process of rock loading and fracturing. This index enables a comprehensive analysis of how the rock undergoes damage evolution throughout the loading and fracturing phases. A higher cumulative ringing count indicates a more severe level of internal damage. As depicted in Fig. 5, initially, there's a minimal occurrence of acoustic emission ringing during the initial loading stage. During the subsequent online elastic deformation phase, there's a gradual increase in the cumulative ringing count. However, as the deformation progresses into the nonlinear stage, there's a rapid escalation in the cumulative ringing count, signifying intensified damage. Upon entering the post-peak deformation stage, fracture development intensifies further, leading to the instability and eventual destruction of the rock sample, culminating in the peak cumulative ringing count.

4. Multivariate functional characterization of "acoustic-thermal-stress" information

The process of loading rock induces responses in various physical fields, including acoustic emission (AE) and infrared radiation (IR), among others. Integrating and analyzing multiple monitoring data such as "acoustic-thermal-stress" not only enhances our understanding of the specimen's rupture process and the ability to identify precursors but also eliminates redundant information across these fields. This integrated approach holds significant importance in deciphering the mechanisms underlying rock rupture and improving precursor detection, thereby aiding in timely warnings.

4.1. Multisource information normalization

Significant variations exist in both the scale and significance of the multivariate monitoring data produced during the rock loading process. This makes it challenging to swiftly, intuitively, and precisely assess the response characteristics of each physical aspect related to rock fracture and joint analysis. Employing a data normalization technique allows for the attainment of dimensionless multivariate information, thereby accentuating the patterns of change across multiple fields. This normalization process enables a more streamlined and insightful understanding of the complex interplay of factors involved in rock mechanics, facilitating more informed decision-making and analysis.

The value domain of rock stress, acoustic emission, and thermal radiation data is denoted as [Min, Max]. Equation (1) shows the mathematical expression for normalizing the linear function.

$$y_u(x) = \frac{x - Min}{Max - Min} \tag{1}$$

In this equation, "u" denotes the count of multivariate parameters. "x" and "y" represent the stress, acoustic emission, and infrared radiation multivariate experimental data, respectively, both before and after undergoing normalization through a linear function. "max" and "min" signify the highest and lowest values within the acoustic emission, infrared radiation, and stress data, respectively.

Fig. 6 illustrates the acoustic, thermal, and stress data of the specimen post-normalization. It is evident from the figure that the underlying interrelationships and trends among the multi-source data persist unchanged following the normalization process via the linear function.

4.2. Multisource information function characterization

The function serves as a powerful tool for quantitatively representing complex information across multiple variables throughout the process of rock loading. By observing shifts in posture and numerical values within this multivariate information function, it elucidates the patterns of change within the information set and reveals correlations between each parameter. This is crucial for effectively analyzing and identifying precursor signals of rock rupture. To accomplish this, we utilize rational functions, Gaussian functions, and polynomials to model the acoustic, thermal, and stress data leading up to the peak loading of rock samples. Through

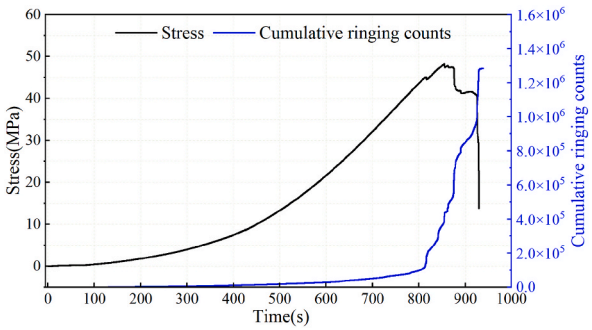

Fig. 5. Relationship curves of stress, cumulative ringing count and time of A_3 specimen.

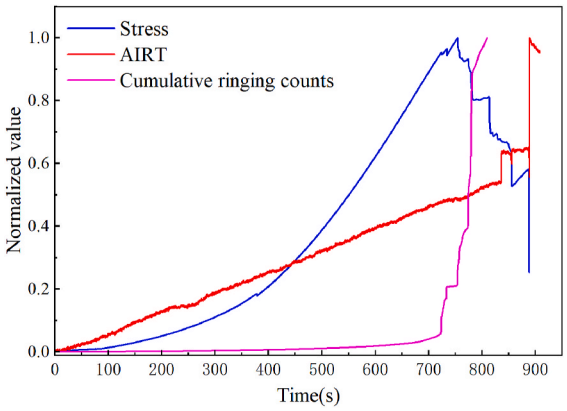

Fig. 6. Normalized values of multi-source data during loading of A_3 specimens.

fitting these functions and assessing correlation coefficients, we determine that rational functions provide a better fit for AIRT data, while Gaussian functions are more suitable for accurately modeling cumulative ringing counts and stress data.

AIRT data were fitted using a rational function. The mathematical expression for the rational function is given in Equation (2).

$$f(x) = \frac{\sum_{j=1}^{n+1} p_j x^{n+1-j}}{x^m + \sum_{j=1}^{m} q_j x^{m-1}} \tag{2}$$

in this context, the function f(x) represents the axial stress experienced during the loading process of the rock specimen. The variables m and n represent the number of occurrences of the highest x term in the denominator and numerator of the rational function, respectively. Additionally, p_j and q_j denote the coefficients associated with the x term. To ensure consistency across different rock samples and maintain a correlation coefficient of at least 0.90 for the fitted curves, m and n are set to 2 and 3, respectively.

A Gaussian function was employed to fit the cumulative ringing counts and stress data. Notably, the second term yielded the highest correlation coefficient among the fitted functions. Equation (3) mathematically represents the Gaussian function.

$$f(x) = \sum_{i=1}^{s} a_i \exp\left(- ((x - b_i)/c_i)^2 \right) \tag{3}$$

The curves after fitting the acoustic, thermal, and stress information for the loading phase before the rock peak using Gaussian and rational functions are shown in Fig. 7.

5. A comprehensive evaluation model for multi-information fusion analysis

5.1. Principal component analysis

The intricate interplay among stress fields, acoustic emissions, temperature variations, and other monitoring parameters constitutes a complex yet informative tapestry that delineates the history and progression of rock fractures. Amidst this intricate web of data, Principal Component Analysis (PCA) emerges as a prominent algorithm celebrated for its prowess in condensing high-dimensional datasets into more digestible forms. By compressing the data's dimensionality while striving to retain its essential features, PCA

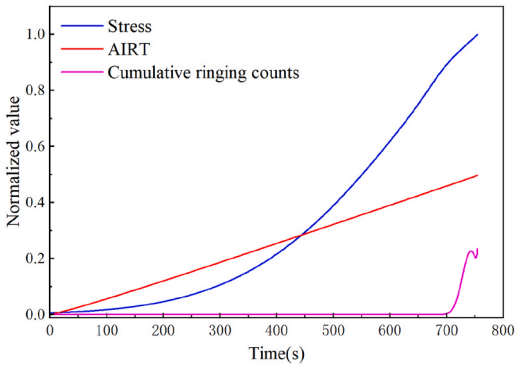

Fig. 7. Gaussian and rational function characterization curves for acoustic, thermal and stress data of A_3 specimen.

offers a pathway to craft a more succinct representation of the original dataset.

This process of dimensionality reduction not only simplifies the convoluted structure of multivariate monitoring data but also facilitates the integration of diverse sources like stress fields, acoustic emissions, and temperature variations. Through this fusion, a comprehensive array of indicators emerges, encapsulating the multifaceted dynamics of rock fracture phenomena. These amalgamated indicators furnish researchers and analysts with a clearer and more comprehensive comprehension of the underlying mechanisms propelling rock fractures forward.

Furthermore, the consolidation of monitoring information into a unified set of indicators not only facilitates the analysis of rock fracture phenomena but also streamlines data processing and interpretation. This streamlined approach enhances the efficiency and accuracy of fracture assessment and prediction methodologies, thus driving advancements in the realms of geosciences and rock mechanics. Hence, PCA serves as an invaluable tool in unraveling the complexities inherent in rock fracture problems, laying the groundwork for innovative solutions and profound insights.

In response to rock rupture, stress, AIRT (Acoustic Impulse Response Technique), and cumulative ringing counts are chosen as the primary analytical indicators of stress, acoustic emission, and temperature fields. The mathematical models derived from stress, acoustic, and thermal data in the preceding section are sampled at regular intervals with a time step of 1 s to construct the sample matrix. This matrix comprises column vectors representing stresses, AIRT, and accumulated ringing counts. Equation (4) mathematically represents the simple matrix of the specimen.

$$F=[X_1,X_2,X_3]=\begin{bmatrix} 0.00604 & -0.00101 & 0 \\ 0.00632 & 0.00111 & 0 \\ \vdots & \vdots & \vdots \\ 0.23581 & 0.49678 & 1 \end{bmatrix} \tag{4}$$

where X_1, X_2, and X_3 denote the column vectors of equal time steps consisting of stress, AIRT, and cumulative ringing counts, respectively. f is a two-dimensional matrix of specimens T × 3, denoting the sample matrix of the specimens. t is the number of rows of the sample matrix, i.e., the maximum number of integer seconds of the experimental duration.

The data were first standardized with a mean of 0 and variance of 1 for each column in the sample matrix. Equation (5) mathematically represents the data standardization.

$$X_i^{'}=\frac{X_i-\mu}{\sigma} \tag{5}$$

Where, μ and σ are the mean and variance of the information values in each column of the sample matrix, respectively. $X_i^{'}$ is the normalized column vector.

The matrix of correlation coefficients was obtained for the sample matrix after specimen standardization. The correlation coefficient matrix for rock sample A_3 is shown Equation (6).

$$\eta=\begin{bmatrix} 1 & 0.9483 & 0.4892 \\ 0.9483 & 1 & 0.3845 \\ 0.4892 & 0.3845 & 1 \end{bmatrix} \tag{6}$$

where, η is the correlation coefficient matrix.

The eigenvalues of the correlation coefficient matrix are derived using the formula outlined in Equation (7). These eigenvalues serve as indicators of the amount of stress, acoustic, and thermal information effectively captured in the rock loading process by the corresponding features. A higher eigenvalue signifies a greater representation of such information. Principal components are then identified based on the criterion that their eigenvalue exceeds 1 or that the cumulative contribution rate of eigenvalues reaches at least 85 %, as expressed in Equation (8). This method ensures the selection of significant components that comprehensively characterize the underlying data patterns.

$$|\eta-\lambda_k E|=0 \tag{7}$$

$$\frac{\sum_{k=1}^{m}\lambda_k}{\sum_{k=1}^{3}\lambda_k}\times 100\% \geq 85\% \tag{8}$$

where, λ_k is the eigenvalue of the correlation coefficient matrix, k = 1, 2, 3. And E is the unit matrix.

Based on the outlined calculation procedure, the eigenvalues and corresponding contribution rates of the correlation coefficient matrix for A3 rock samples were computed, and the results are presented in Table 1. Due to space constraints, the correlation coefficient matrix and contribution rates for all rock samples are not provided here; however, the same methodology was applied to the remaining rock samples. By adhering to the criterion that the cumulative contribution rate exceeds 85 %, it is deduced that two principal components effectively capture the multicomponent behavior during the rock loading process. In essence, this implies that:

$$g_1 = a_{11}X_1 + a_{12}X_2 + a_{13}X_3 \tag{9}$$

$$g_2 = a_{21}X_1 + a_{22}X_2 + a_{23}X_3 \tag{10}$$

where g_1 and g_2 are the function models corresponding to the two principal components, and X_1, X_2 and X_3 are the stress, AIRT and cumulative ringing counts, respectively. a_{ij} (i = 1, 2; j = 1, 2, 3) denotes the factor loading coefficients corresponding to the two principal components. From Eqs. (9) and (10), the integrated rock evaluation model can be obtained as:

$$g = \frac{s_1}{s_1 + s_2}g_1 + \frac{s_2}{s_1 + s_2}g_2 \tag{11}$$

where g denotes the integrated evaluation model of load-bearing rocks, and s_1 and s_2 denote the contribution of principal component 1 and principal component 2, respectively.

Based on Eqs. (9)–(11), Equation (12) shows comprehensive evaluation model.

$$g = 0.4342X_1 + 0.3840X_2 + 0.5493X_3 \tag{12}$$

Fig. 8 illustrates the weight coefficients assigned to each parameter in the comprehensive evaluation model for individual samples. Upon observing the overall distribution, it becomes evident that the weight coefficient attributed to the cumulative ringing count stands out as the most significant, followed by AIRT and stress, respectively. Consequently, the order of specimen failure strength can be deduced as follows: cumulative ring count holds the highest significance, succeeded by AIRT and stress.

To elaborate further, a comprehensive evaluation model for assessing the damage incurred by uniaxially loaded rock was devised utilizing stress, acoustic, and thermal data through the principal component analysis method. The essence of this model lies in the cumulative aggregation of stress, acoustic emission, and infrared radiation parameters, each multiplied by their respective weights. This model serves as a crucial reference point for the monitoring and early detection of potential rock fracture instability, offering valuable insights into preventive measures.

5.2. Multi-information fusion for early warning and probability of rock fracture precursors

The turning point in the state of rock damage occurs when the posture of the function curve changes at the extreme value point and the stationary point. This pivotal moment in rock fracture evolution is crucially indicated by the nonlinear shifts in the multivariate monitoring information function, as illustrated in Fig. 6. These extreme and stationary points serve as fundamental markers for delineating different stages of rock fracture evolution. This study employs a rational function to effectively model the comprehensive evaluation curve. Notably, the best fitting is achieved using a rational function with a denominator of 2 and a constant term as the numerator, yielding a fitting correlation coefficient of at least 0.95. Fig. 9 depicts the fitting curve, along with the first-order and second-order derivative curves of the comprehensive evaluation model for all five rock samples. The first-order derivative holds physical significance as it denotes the rate of change of the comprehensive evaluation model curve, providing insight into the model's sensitivity to the rock loading rupture process. The extremum of the first-order derivative signifies a transition in sensitivity state, indicating critical shifts in the rock's response to loading.

As depicted in Fig. 9, the curves obtained from the comprehensive rock evaluation model exhibit a distinctive pattern characterized by an initial rapid increase followed by a gradual ascent, while the first-order derivative curves take on an inverted "V" shape. This inverted "V" shape is indicative of critical points in the rock samples' behavior. The specific timing and stress levels corresponding to these critical points for each rock sample are detailed in Table 2. For instance, rock samples A_1, A_2, A_3, A_4, and A_5 reach their extreme points at 686s, 724s, 656s, 872s, and 507s, respectively, with corresponding stress levels of 0.78 σ_{max}, 0.72 σ_{max}, 0.77 σ_{max}, 0.93 σ_{max}, and 0.65 σ_{max}. Upon averaging, the precursor stress level is determined to be 0.77 σ_{max}. Consequently, the extreme value point identified in the first-order derivative function of the comprehensive evaluation model serves as a crucial precursor warning point for rock damage.

This paper defines the rupture period as the interval encompassing the loading phase from the initiation of rupture to the attainment of peak stress, aiming to comprehensively scrutinize the damage characteristics of rocks. Identifying the damage precursor serves as a pivotal reference for temporal monitoring and preemptive measures against potential rock engineering hazards. Furthermore, delving into the rupture period facilitates the monitoring of the metamorphic progression of rocks. Utilizing the energy superposition method, the post-rupture phase in rock behavior is construed as an aggregation of acoustic emission and infrared radiation data energy. As the energy accumulation approaches its threshold, represented by the peak stress, the load-bearing capacity of the rock progressively diminishes. By employing the energy superposition method, this study derives expressions for the energy of acoustic emission and infrared radiation data during the rupture period.

Table 1
Characteristic value and contribution rate of sample A_3.

η_{A3} eigenvalue	rate of contribution (%)	Cumulative contribution rate (%)
2.2534	75.1143	75.1143
0.7022	23.4050	98.5193
0.444	4.4807	100

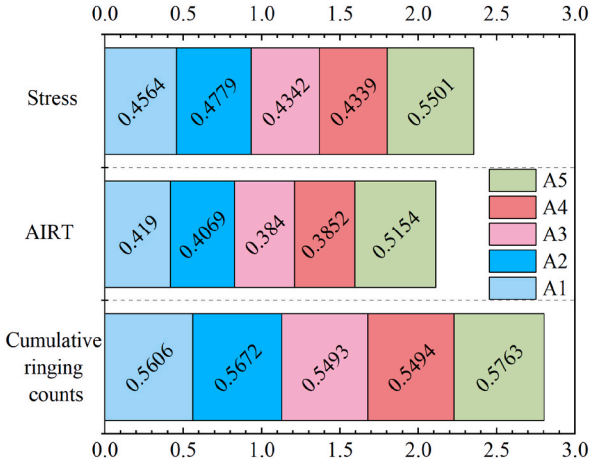

Fig. 8. Coefficient of comprehensive evaluation model.

$$E(t) = \sum_{0}^{t} (a_1 X_1 + a_2 X_2 + a_3 X_3)^2 \tag{13}$$

in equation (13), E(t) is the total energy of the acoustic-thermal-force information during the rock rupture period, and t is the rupture time. X_1, X_2, X_3 are the time-dependent acoustic-thermal-force parameters.

The total energy expression of "acoustic-thermal-force" information in the rupture phase is taken as the probability density value. According to the formula of probability theory and mathematical statistics probability distribution function, the expression of damage probability in the rupture stage of rock samples is:

$$P(t) = \frac{\int_0^t E(x)dx}{\int_0^T E(x)dx} \tag{14}$$

where P(t) is the probability of destruction of the rock specimen at any moment during the rupture process and T is the time corresponding to the peak stress.

At the instant when time (T) equals 't', the rock reaches its maximum stress-bearing capacity. Subsequently, during the post-peak deformation phase, the rock's ability to bear stress steadily diminishes, and at the peak stress point, the probability of rock specimen damage is confirmed as 1. Utilizing Equation (14), the damage probability density curve of the rock specimen is computed. As depicted in Fig. 10, the progression of the rock's damage probability, as per the comprehensive evaluation model, demonstrates an almost exponential growth trajectory. Specifically, the damage probability of specimen A3 during the initial phase of rupture registers at 0.44. By scrutinizing the evolution of the damage probability curve throughout the rupture period, it becomes feasible to ascertain the damage probability of the rock at any given moment during this period.

6. Discussion

The variation of infrared temperature on the surface of rocks is a comprehensive response to rock deformation and fracturing [54]. Scholars have categorized it into factors such as gas escape, thermoelastic effect, and crack propagation thermal effect. These factors have varying degrees of influence at different stages, collectively resulting in changes in the demonstrated surface infrared radiation temperature. it is represented by Equation (15).

$$\Delta T = \Delta T_1 + \Delta T_2 + \Delta T_3 \tag{15}$$

In the equation, ΔT represents the change in infrared temperature on the surface of rocks, while ΔT_1 represents the change in infrared temperature caused by the thermoelastic effect on the rocks. This effect is related to the stress state of the rock during the elastic deformation stage [54,55] and can be shown mathematically, as given in Equation (16).

$$\Delta T_1 = \gamma \beta^{-1} T \Delta(\sigma_1 + \sigma_2 + \sigma_3) \tag{16}$$

where, T represents the physical temperature of the rock, γ denotes the transfer factor, and β is a constant related to the emissivity of the rock surface and thermoelastic effect. σ_1, σ_2, and σ_3 respectively represent the first, second, and third principal stresses.

ΔT_2 represents the temperature change caused by the initial crack propagation and the generation of new cracks, which consumes energy. Meanwhile, ΔT_3 represents the temperature change on the rock surface caused by the heat generated from the friction between internal cracks, microcracks, and mineral crystal particles under external loading.

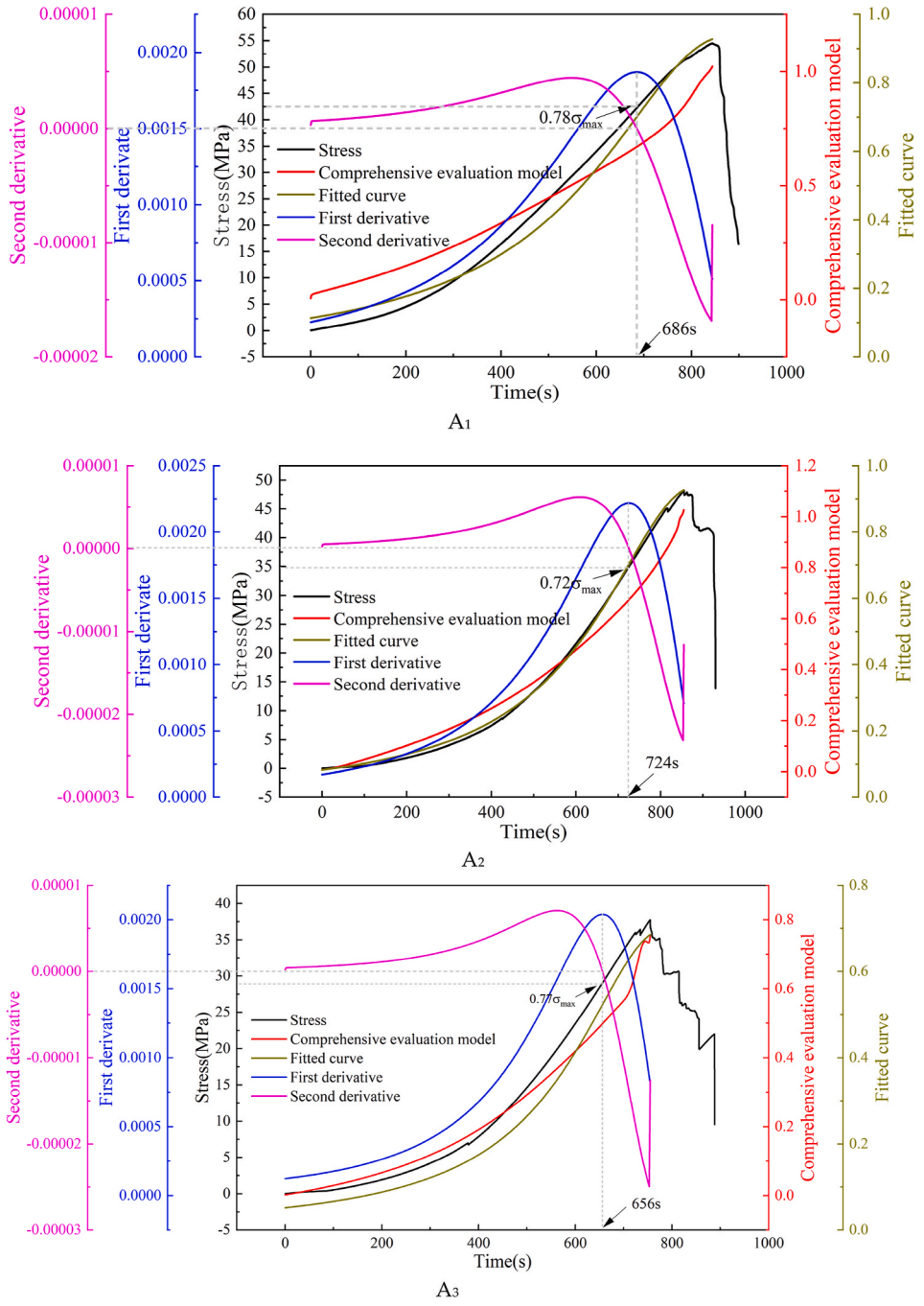

Fig. 9. Fitting curve and derivative curve of the comprehensive evaluation model.

The three components mentioned above are various phenomena resulting from the interaction between the internal state and stress state of the rock itself, which converge to the changes in infrared temperature on the rock surface. This also involves the internal temperature transfer mechanism, where the temperature of each position on the rock surface is influenced by the temperatures at various positions inside the rock [28,56].

Rock damage represents a complex nonlinear process primarily induced by underground engineering activities. The intricacy of this destructive process is further exacerbated by the diverse environmental factors surrounding it, including water, gas, and impact ground pressure. Initial defects within rocks, such as micropores and microcracks, serve as the starting points for damage, gradually intensifying under external forces. This progression causes the stress-strain relationship of the material unit to deviate from its linear

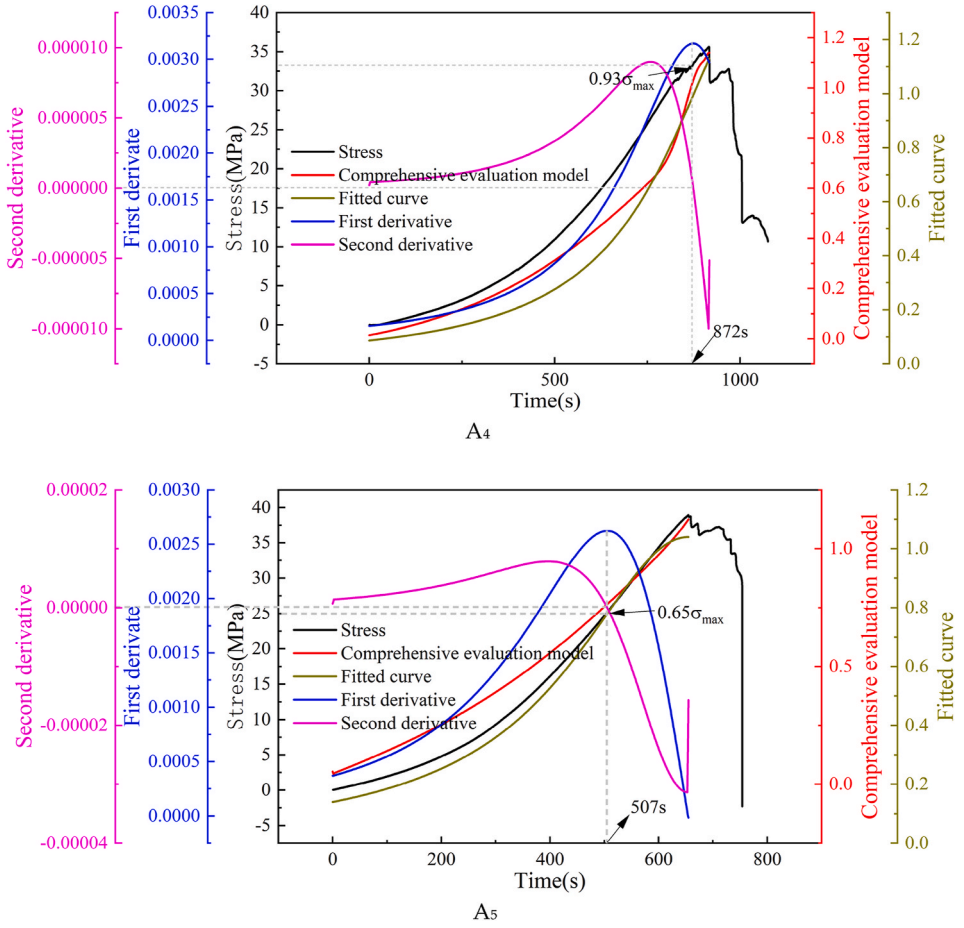

Fig. 9. (*continued*).

Table 2
Statistical parameters of rock samples.

Sample number	Peak stress/Mpa	Peak stress time/s	Elastic modulus/Gpa	Time corresponding to the maximum point of the first derivative/s	Maximum point corresponds to stress/Mpa	Maximum point stress level
A_1	54.50	843.3	4.8	686	42.35	0.78
A_2	48.25	854.9	2.98	724	34.86	0.72
A_3	37.73	754.7	3.08	656	29.03	0.77
A_4	35.62	916	2.62	872	33.264	0.93
A_5	38.92	654.9	3.94	507	25.364	0.65

nature, ultimately manifesting the fundamental property of nonlinearity [57].

The nonlinear characteristics inherent in rocks contribute to the amplification of rupture behavior variability, resulting in the release of multi-physical field information during the rupture process. This complexity and variability pose significant challenges to safety monitoring efforts. Furthermore, various physical field information is influenced by distinct environmental conditions. Hence, the approach of multivariate information fusion analysis emerges as a promising methodology for field applications, promising improved adaptability of fused information to the work site environment, as well as enhanced robustness and reliability of monitoring and warning outcomes [33,58].

In light of these challenges, it becomes imperative to thoroughly consider the influence of multiple physical factors on monitoring effectiveness in future research endeavors. The authors plan to delve into exploring the fracture damage characteristics of rocks using a combination of research methods, including rock fine-scale damage mechanics and probabilistic statistical approaches. The objective is to establish a comprehensive multi-physics field model that reflects the nonlinearity, randomness, and coupling effects inherent in the rock damage evolution process. Such a model will not only advance our understanding of rock damage but also provide crucial guidance for safety monitoring and early warning systems in diverse engineering fields, including mining and geotechnical applications.

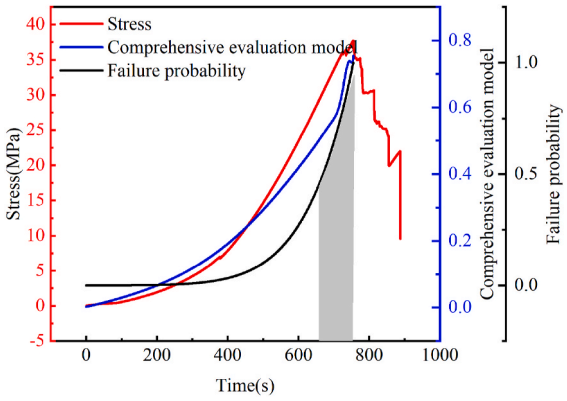

Fig. 10. Evolution curve of rupture probability of A_3 specimen.

7. Conclusions

The following conclusion are drawn.

- Through the application of Principal Component Analysis (PCA), this research has successfully developed a comprehensive evaluation model that quantifies the influence of acoustic emission indicators, infrared radiation indicators, and stress on the rock loading rupture process. This model provides a robust theoretical framework for the identification of rock rupture precursors. The model reveals that the sensitivities of the physical fields to the damage response of rock specimens, in descending order, are cumulative ringing counts, AIRT, and stress.
- Addressing the variability in the response of individual physical fields to the rupture of loaded rocks, this study introduces a novel approach to pinpointing the precursors of rock damage. By identifying the extreme value point of the first-order derivative function from the "acoustic-thermal-force" comprehensive evaluation model as the warning sign of imminent rock damage, the method has determined that the average stress level at which these rupture precursors occur is $0.77\sigma_{max}$.
- This research further explores the "acoustic-thermal-force" information fusion analysis during the rupture phase of rocks, from the onset of rupture precursors to the peak stress. An expression for the total energy of the integrated "sound-heat-force" information has been formulated based on the energy superposition method. This allows for the determination of the probability density of rock damage at any given moment within the rupture period, thus achieving a probabilistic warning system for rock rupture.

Data availability statement

Data will be made available on request.

Funding

This paper was supported by the Research and Engineering Demonstration of Low Cost Large Scale Purification and Cascade Utilization Technology for Mining Brackish Water in the Zhundong Region (2023B03009), the Postgraduate Research & Practice Innovation Program of Jiangsu Province (KYCX23_2811), the Graduate Innovation Program of China University of Mining and Technology (2023WLKXJ046) and the Researchers Supporting Project number (RSP2024R496), King Saud University, Riyadh, Saudi Arabia.

CRediT authorship contribution statement

Qiangqiang Gao: Writing – review & editing, Writing – original draft, Methodology, Funding acquisition, Formal analysis, Conceptualization. **Liqiang Ma:** Writing – review & editing, Writing – original draft, Methodology, Funding acquisition, Formal analysis, Conceptualization. **Wei Liu:** Writing – original draft, Methodology, Funding acquisition, Formal analysis, Conceptualization. **Naseer Muhammad Khan:** Writing – review & editing, Methodology, Formal analysis, Conceptualization. **Saad S. Alarifi:** Writing – original draft, Validation, Software, Resources, Data curation. **Mohammed Sazid:** Writing – review & editing, Validation, Supervision, Resources, Investigation, Formal analysis, Data curation. **Waleed Bin Inqiad:** Writing – original draft, Software, Methodology, Conceptualization.

Declaration of competing interest

The authors declare that they have no known competing financial interests or personal relationships that could have appeared to

influence the work reported in this paper.

References

[1] S. Dong, W. Zhou, H. Wang, Introduction to special issue on mine water Inrushes: risk assessment, mitigation, and prevention, Mine Water Environ. 40 (2) (2021) 321–323.
[2] D. Bai, et al., Using electrical resistivity tomography to monitor the evolution of landslides' safety factors under rainfall: a feasibility study based on numerical simulation, Rem. Sens. 14 (15) (2022) 3592.
[3] S. He, et al., Early warning of coal dynamic disaster by precursor of AE and EMR" quiet period", Inter. J Coal Sci. Technol. 9 (1) (2022) 46.
[4] Y.-k. Ma, et al., Mechanism investigation on coal and gas outburst: an overview, Int. J. Miner. Metall. Mater. 27 (2020) 872–887.
[5] T. Hao, et al., Infrared precursor of pre-cracked coal failure based on critical slowing down, Geomatics, Nat. Hazards Risk 13 (1) (2022) 1682–1699.
[6] Y. Liang, et al., Study on the acoustic emission and thermal infrared signal characteristics of granite with freeze-thaw damage in cycle loading process, Front. Earth Sci. 10 (2022).
[7] X.X. Liu, et al., Experimental study on the monitoring of rockburst in tunnels under dry and saturated conditions using AE and infrared monitoring, Tunn. Undergr. Space Technol. 82 (2018) 517–528.
[8] H. Sun, et al., Experimental investigation of acoustic emission and infrared radiation thermography of dynamic fracturing process of hard-rock pillar in extremely steep and thick coal seams, Eng. Fract. Mech. (2020) 226.
[9] P. Boral, A.K. Varma, S. Maity, Nitration of Jharia basin coals, India: a study of structural modifications by XRD and FTIR techniques, Inter. J. Coal Sci. Technol. 8 (5) (2021) 1034–1053.
[10] A. Nádudvari, et al., Classification of fires in coal waste dumps based on Landsat, Aster thermal bands and thermal camera in Polish and Ukrainian mining regions, Inter. J. Coal Sci. Technol. 8 (3) (2021) 441–456.
[11] L.X. Wu, et al., Remote sensing rock mechanics (RSRM) and associated experimental studies, Int. J. Rock Mech. Min. Sci. 37 (6) (2000) 879–888.
[12] L. Wu, et al., Changes in infrared radiation with rock deformation, Int. J. Rock Mech. Min. Sci. 39 (6) (2002) 825–831.
[13] L.X. Wu, et al., Experimental study on infrared anomaly of tectonic earthquake, Rem. Sens. Environ. Monit., Gis Appl., Geology III 5239 (2004) 376–387.
[14] L.X. Wu, et al., Precursors for rock fracturing and failure—Part II: IRR T-Curve abnormalities, Int. J. Rock Mech. Min. Sci. 43 (3) (2006) 483–493.
[15] L.Q. Ma, et al., Characteristics of infrared radiation of coal specimens under uniaxial loading, Rock Mech. Rock Eng. 49 (4) (2016) 1567–1572.
[16] W.Z. Shi, Y.H. Wu, L.X. Wu, Quantitative analysis of the projectile impact on rock using infrared thermography, Int. J. Impact Eng. 34 (5) (2007) 990–1002.
[17] K. Zhang, et al., Quantitative description of infrared radiation characteristics of preflawed sandstone during fracturing process, J. Rock Mech. Geotech. Eng. 13 (1) (2021) 131–142.
[18] L. Ma, et al., An experimental study on infrared radiation characteristics of sandstone samples under uniaxial loading, Rock Mech. Rock Eng. 52 (2019) 3493–3500.
[19] M.A. Liqiang, et al., Characteristics on the variance of differential infrared image sequence during coal failures under uniaxial loading, Chin. J. Rock Mech. Eng. 36 (2017) 3927–3934.
[20] Q. Gao, et al., Appraisal of rock IR law and damage precursor: insight infrared thermogram entropy, Infrared Phys. Technol. (2022) 104443.
[21] W. Liu, et al., Using the characteristics of infrared radiation b-value during the rock fracture process to offer a precursor for serious failure, Infrared Phys. Technol. 114 (2021) 103644.
[22] K. Cao, et al., An experimental study of infrared radiation characteristics of sandstone in dilatancy process, Int. J. Rock Mech. Min. Sci. 136 (2020) 104503.
[23] T. Shan, et al., Infrared radiation and acoustic emission of damage evolution and failure precursory for water-bearing coal, Rock Mech. Rock Eng. 55 (12) (2022) 7657–7674.
[24] S. Liu, et al., Quantitative analysis methods of infrared radiation temperature field variation in rock loading process, Chin. J. Rock Mech. Eng. 34 (9) (2015).
[25] X. Cai, et al., Water saturation effects on thermal infrared radiation features of rock materials during deformation and fracturing, Rock Mech. Rock Eng. 53 (11) (2020) 4839–4856.
[26] Z.H. Li, et al., Experimental study on the infrared thermal imaging of a coal fracture under the coupled effects of stress and gas, J. Nat. Gas Sci. Eng. 55 (2018) 444–451.
[27] S. Mineo, G. Pappalardo, Infrared thermography presented as an innovative and non-destructive solution to quantify rock porosity in laboratory, Int. J. Rock Mech. Min. Sci. 115 (2019) 99–110.
[28] W. Liu, et al., Fracture precursor recognition and damage quantitative characterization of stressed rock using infrared radiation, Rock Mech. Rock Eng. 56 (8) (2023) 5567–5584.
[29] K. Ohno, M. Ohtsu, Crack classification in concrete based on acoustic emission, Construct. Build. Mater. 24 (12) (2010) 2339–2346.
[30] M.M. Wang, et al., Crack classification and evolution in anisotropic shale during cyclic loading tests by acoustic emission, J. Geophys. Eng. 14 (4) (2017) 930–938.
[31] Q.B. Meng, et al., Effects of acoustic emission and energy evolution of rock specimens under the uniaxial cyclic loading and unloading compression, Rock Mech. Rock Eng. 49 (10) (2016) 3873–3886.
[32] P. Shan, X. Lai, X. Liu, Correlational analytical characterization of energy dissipation-liberation and acoustic emission during coal and rock fracture inducing by underground coal excavation, Energies 12 (12) (2019) 2382.
[33] Z. Ding, et al., Feature extraction, recognition, and classification of acoustic emission waveform signal of coal rock sample under uniaxial compression, Int. J. Rock Mech. Min. Sci. 160 (2022) 105262.
[34] N.M. Khan, et al., Early violent failure precursor prediction based on infrared radiation characteristics for coal specimens under different loading rates, Rock Mech. Rock Eng. 55 (11) (2022) 6939–6961.
[35] P. Liu, et al., A potential mechanism of the satellite thermal infrared seismic anomaly based on change in temperature caused by stress variation: theoretical, experimental and field investigations, Rem. Sens. 14 (22) (2022).
[36] R. Shen, et al., Study on the effect of the lower limit of cyclic stress on the mechanical properties and acoustic emission of sandstone under cyclic loading and unloading, Theor. Appl. Fract. Mech. 108 (2020) 102661.
[37] T.H. Ma, et al., Rockburst mechanism and prediction based on microseismic monitoring, Int. J. Rock Mech. Min. Sci. 110 (2018) 177–188.
[38] T. Zhao, et al., Master Crack Types and Typical Acoustic Emission Characteristics during Rock Failure, vol. 10, 2023, p. 1.
[39] A. Kirmaci, M. Erkayaoglu, Thermographic analysis of failure for different rock types under uniaxial loading, Geomechanics and Engineering 23 (6) (2020) 503–512.
[40] H.Q. Yang, B.L. Liu, S. Karekal, Experimental investigation on infrared radiation features of fracturing process in jointed rock under concentrated load, Int. J. Rock Mech. Min. Sci. 139 (2021) 104619.
[41] B. Liu, et al., Characteristic strength and acoustic emission properties of weakly cemented sandstone at different depths under uniaxial compression, Inter. J. Coal Sci. Technol. 8 (2021) 1288–1301.
[42] D. Xue, et al., Cluster modeling of the short-range correlation of acoustically emitted scattering signals, Inter. J. Coal Sci. Technol. 8 (4) (2021) 575–589.
[43] C. Zhou, et al., Thermal infrared imagery integrated with multi-field information for characterization of pile-reinforced landslide deformation, Sensors 20 (4) (2020).
[44] S. Li, et al., Multi-sources information fusion analysis of water inrush disaster in tunnels based on improved theory of evidence, Tunn. Undergr. Space Technol. 113 (2021) 103948.
[45] B. Li, et al., Optimize the early warning time of coal and gas outburst by Multi-source information fusion method during the tunneling process, Process Saf. Environ. Protect. 149 (2021) 839–849.

[46] W. Shen, S. Zhang, C. Li, Research of experimental modal analysis and multi-information fusion applied in structural damage detection, in: 2010 International Conference on Digital Manufacturing & Automation, IEEE, 2010.
[47] Q. Gao, et al., Research on the denoising method of infrared thermogram during rock fracture, Infrared Phys. Technol. (2023) 104651.
[48] T. Shan, et al., Infrared radiation and acoustic emission of damage evolution and failure precursory for water-bearing coal, Rock Mech. Rock Eng. 55 (12) (2022) 7657–7674.
[49] L.X. Wu, et al., Precursors for rock fracturing and failure - Part I: IRR image abnormalities, Int. J. Rock Mech. Min. Sci. 43 (3) (2006) 473–482.
[50] N.-F. Deng, et al., A method to predict rock fracture with infrared thermography based on heat diffusion analysis, Geofluids (2021) 2021.
[51] K. Zhang, et al., Quantitative description of infrared radiation characteristics of preflawed sandstone during fracturing process, J. Rock Mech. Geotech. Eng. 13 (1) (2020).
[52] Z. Yang, S.-Q. Yang, M. Chen, Peridynamic simulation on fracture mechanical behavior of granite containing a single fissure after thermal cycling treatment, Comput. Geotech. 120 (2020).
[53] S. Song, et al., Fracture features of brittle coal under uniaxial and cyclic compression loads, Inter. J. Coal Sci. Technol. 10 (1) (2023) 9.
[54] L. Wu, et al., Precursors for rock fracturing and failure—Part I: IRR image abnormalities, Int. J. Rock Mech. Min. Sci. 43 (3) (2006) 473–482.
[55] S.J. Liu, L.X. Wu, Y.H. Wu, Infrared radiation of rock at failure, Int. J. Rock Mech. Min. Sci. 43 (6) (2006) 972–979.
[56] W. Liu, et al., An experimental study on infrared radiation and acoustic emission characteristics during crack evolution process of loading rock, Infrared Phys. Technol. 118 (2021) 103864.
[57] Y. Chen, et al., Experimental and numerical study of coal-rock bimaterial composite bodies under triaxial compression, Inter. J. Coal Sci. Technol. 8 (5) (2021) 908–924.
[58] Y. Di, et al., Comprehensive early warning method of microseismic, acoustic emission, and electromagnetic radiation signals of rock burst based on deep learning, Int. J. Rock Mech. Min. Sci. 170 (2023) 105519.